Folded acoustic phonons in Si/Ge_xSi_{1-x} strained-layer superlattices

D. J. Lockwood, M. W. C. Dharma-wardana, J. -M. Baribeau, and D. C. Houghton
Division of Physics, National Research Council, Ottawa, Canada K1A 0R6
(Received 19 August 1986)

We present a detailed Raman scattering study of folded longitudinal acoustic modes in Si/Ge_xSi_{1-x} strained-layer superlattices with $0.2 \leq x < 0.5$. Rytov's theory of acoustic vibrations in layered media was found to model accurately the observed Raman line frequencies and intensities. Studies of large-period ($d \geq 275$ Å) superlattices, where the scattering wave vector of the photon lies outside the mini-Brillouin-zone, have allowed observation of umklapp-mediated Brillouin and Raman lines involving the folding of the photon wave vector.

I. INTRODUCTION

Raman scattering from semiconductor superlattices made up of alternating layers of $GaAs/Al_xGa_{1-x}As$ has received much attention for several reasons. Raman scattering provides a rapid means of characterizing a superlattice and also provides a technique for studying the "folding" of the phonon dispersion in the reduced (or mini) Brillouin zone caused by the new periodicity d of the superlattice.[1-5] In a recent Rapid Communication[6] we reported Raman scattering studies of phonon folding in molecular-beam epitaxy (MBE) grown Si/Ge_xSi_{1-x} strained-layer superlattices. Using superlattices with thick layers (hence large d) the mini-Brillouin-zones were reduced to such an extent that umklapp processes could be observed. Here we give a more detailed account of Raman scattering from strained layer Si/Ge_xSi_{1-x} superlattices grown by MBE on (001) Si substrates.

In this paper we consider only the scattering from folded acoustic phonons. The folded optic modes were not resolvable in these experiments. Six MBE-grown samples, labeled MBE-17, -26, -35, -37, -43, and -44 were studied, with varying periodicities and germanium composition. For suitable samples, the momentum transferred from the photon, $\mathbf{q}_p$, could be made to probe internal or external regions of the minizone by changing the experimental conditions. In the following section (Sec. II) we outline the theory, which is based on Rytov's model of acoustic wave propagation in layered media. In Sec. III experimental details are given. This is followed by a discussion of the spectra of the various samples in Sec. IV and the conclusions in Sec. V.

II. RYTOV'S MODEL FOR FOLDED ACOUSTIC PHONONS

A number of different approaches to modeling phonons in superlattices have been proposed, the most comprehensive so far being that of Yip and Chang.[7] In Refs. 2 and 4 several models were compared and it was concluded that Rytov's elastic wave model was adequate for describing acoustic phonons in GaAs/AlAs superlattices with, say, more than ten atomic layers per period. This is expected to hold true for Si/Ge_xSi_{1-x} superlattices as well. Since the superlattices studied by us contain *over 70* atomic layers per period (smallest $d \approx 200$ Å), and since the Raman frequency shifts were less than 75 cm^{-1}, we have adopted the Rytov model.[8]

In a superlattice made up of alternating layers of Si of thickness d_1 and Ge_xSi_{1-x} of thickness d_2, the new periodicity $d = d_1 + d_2$ along the growth direction [001] leads to a minizone with the [001] zone edge at π/d, instead of $\pi/(a/2)$, as in the bulk crystal where the lattice parameter $a = 5.43$ Å for Si and 5.65 Å for Ge. Thus the longitudinal acoustic branch that extended from $q_{[001]} = 0$ to $2\pi/a$ in the bulk crystal is folded back into $q_{[001]} = 0$ to π/d, giving many branches which intersect the $q = 0$ axis. This simple construction of the phonon branches in the superlattice by "folding" applies to situations where the elastic properties of the two materials are similar. For large d and for frequencies less than 100 cm^{-1} the dispersion is assumed to be linear and the folded phonons can be described by

$$\omega = \omega_0 m \pm V_{SL} q \ , \qquad \omega_0 \simeq V_{SL}(2\pi/d) \ , \tag{1}$$

where the folding index $m = 0, 1, 2, \ldots$, with $m = 0$ corresponding to the acoustic branch, and q being the superlattice wave vector. The acoustic velocity in the superlattice, V_{SL}, is given in Rytov's theory by

$$V_{SL} = d\left[\frac{d_1^2}{V_1^2} + \frac{d_2^2}{V_2^2} + \left[R + \frac{1}{R}\right]\frac{d_1 d_2}{V_1 V_2}\right]^{-1/2} , \qquad R = \rho_2 V_2 / \rho_1 V_1 \ , \tag{2}$$

where V_1 and V_2, ρ_1 and ρ_2 are the sound velocities and densities for the Si and Ge_xSi_{1-x} alloy layers, respectively. Equation (2) results from Rytov's more complete dispersion relation

$$\cos(qd) = \cos\left[\frac{\omega d_1}{V_1}\right]\cos\left[\frac{\omega d_2}{V_2}\right] - \frac{1}{2}\left[R + \frac{1}{R}\right]\sin\left[\frac{\omega d_1}{V_1}\right]\sin\left[\frac{\omega d_2}{V_2}\right] , \tag{3}$$

where q is the superlattice wave vector perpendicular to

the layers and ω is the circular frequency of the superlattice phonons. Rytov's theory also predicts the formation of minigaps so that Eq. (1) is only an approximation valid when the minigaps are negligible. The minigaps at $q=0$ are approximately given by[4]

$$\Delta\omega_m \propto v \left[\frac{\rho_2-\rho_1}{\rho d}\right] \sin\left[\frac{2m\pi d_1}{d}\right], \tag{4}$$

where v and ρ are "virtual crystal" values for the sound velocity and the density. Hence, for thick-layer crystals (large d) Eq. (1) is an excellent approximation.

The two branches ($\mp q$), viz., m_a and m_b, associated with a given folding index m are assigned to the A_1 and B_2 irreducible representations in Refs. 1, 2, and 4. A more detailed discussion of the group theory of the phonon branches is found in Ref. 3, where it is shown that for $q\neq 0$ the B_2 modes and the A_1 modes mix, the pure B_2 behavior being valid only for $q\rightarrow 0$. This is of some importance since the symmetry determines the selection rules, and hence the intensities of the lines observed in a given experimental geometry.

The experimental arrangement (to be discussed below) involves a right angle scattering geometry, which is effectively a backscattering geometry inside the superlattice owing to the high refractive indices of the materials under study. The component of the scattering wave vector perpendicular to the layers is given by

$$q_p \simeq \frac{4\pi\eta(\lambda)}{\lambda}\left[1-\frac{1}{4[\eta(\lambda)]^2}\right], \tag{5}$$

where λ is the incident laser light wavelength and $\eta(\lambda)$ the refractive index of the material at that wavelength. Then we have

$$\begin{aligned} &q_p = q_{\rm ph} \pm nG_{mz}, \quad n=0,1,\ldots, \\ &G_{mz}=2\pi/d\ , \end{aligned} \tag{6}$$

where $q_{\rm ph}$ is the wave vector of the scattered phonon and G_{mz} is the reciprocal lattice vector in the direction of the superlattice periodicity. If $n\neq 0$ we have scattering with umklapp; note that it is the photon wave vector which is "folded" in this process. Such an umklapp condition cannot be realized in bulk crystals since $q_p \ll q_{\rm BZ}$. However, superlattices can be made such that $q_p > q_{mz}$ and umklapp scattering should occur, as reported in this study.

When q_p is greater than q_{mz}, the reduced scattering momentum $\tilde{q}_p$ is obtained, as in Eq. (6), by adding a suitable reciprocal lattice vector G_{mz}. The resulting $\tilde{q}_p$, with $0\leq\tilde{q}_p\leq\pi/d$, is constructed by writing $q_p/q_{mz}=n+f$, where n is an integer and f the fractional part. Then

$$\tilde{q}_p/q_{mz} = R+(-1)^n f\ , \tag{7}$$

where

$R=0$ for n even ,

$R=1$ for n odd .

This "folding over" of the q vector is essentially the literal meaning of the German word "umklapp."

An important question regarding Raman scattering from superlattices concerns the microscopic details of the scattering contributions to the photoelastic constants in these materials. These constants are often poorly known, both theoretically and experimentally. In terms of the established mechanism for light scattering in superlattices,[4] the Si/Ge_xSi_{1-x} system has less favorable photoelastic constants than GaAs/AlAs,[9] but the Raman scattering from the folded phonons is still readily observable. The Ge_xSi_{1-x} alloy layers of Si/Ge_xSi_{1-x} superlattices are well known as being strongly strained.[10] Hence the atomic positions would be displaced from the minima of the potential wells. Thus, in addition to the usual scattering contributions of the unstrained materials, one may expect modifications in the photoelastic tensor due to changes in the electron screening of phonons as well as multiphonon effects. Such effects may possibly augment the differences in the photoelastic constants for Si and the alloy, thus intensifying the Raman scattering from these strained-layer superlattices.

The density ρ_2 and the acoustic velocity V_2 in the Ge_xSi_{1-x} layers are needed to calculate the theoretical spectrum using Rytov's model. In the present study we have used a linear interpolation between pure-Si and pure-Ge values taken to be $\rho_{\rm Si}=2.33$ g/cm^3, $\rho_{\rm Ge}=5.36$ g/cm^3 and $V_{\rm Si}=8.44\times10^5$ cm/s, $V_{\rm Ge}=4.90\times10^5$ cm/s. The spectra calculated on the basis of the linear-interpolation model agreed very well (see Sec. IV) with the experimental data obtained for our samples where $x<0.5$. On the other hand, in a recent study of acoustic phonons in Si/Ge_xSi_{1-x} superlattices with $x=0.5$, Brugger *et al.*[11] used a slightly higher value for V_2 than that given by the linear-interpolation model. They estimated V_2 by fitting the theoretical doublet splitting $2q_pV_{\rm SL}$ to the observed value for three samples.

III. EXPERIMENTAL

Several Si/Ge_xSi_{1-x} superlattices of various thickness and composition were deposited on (100) Si substrates in a Vacuum Generator V80 MBE system. The layers were grown at temperatures below 550°C and the base pressure in the UHV system was less than 10^{-10} Torr. The relevant parameters of the superlattices are summarized in Table I. The superlattices were assessed by Rutherford backscattering (RBS) channeling, conventional x-ray diffraction, and cross-sectional transmission electron microscopy (TEM). The epitaxial material was of excellent crys-

TABLE I. Physical data for the Si/Ge_xSi_{1-x} superlattices.

MBE sample number	Number of periods	d (Å)	d_1 (Å)	d_2 (Å)	x
35	40	185	145	40	0.30
43	30	185	92	93	0.20
44	20	205	102	103	0.20
17	21	275	225	50	0.20
37	20	410	300	110	0.45
26	21	650	450	200	0.33

talline quality, as confirmed by RBS where χ_{min}'s $\lesssim 4\%$ were obtained. In all the superlattices, the Si/Ge_xSi_{1-x} interfaces were commensurate as revealed by TEM. The sharpness of the interfaces and the absence of dislocations is apparent in the [110] TEM cross-section micrograph of Fig. 1 obtained from sample MBE-44. The accompanying selected-area diffraction pattern shows the typical satellite spots associated with the superlattice periodicity of about 200 Å. In Si/Ge_xSi_{1-x} superlattices grown on (100) Si, the lattice mismatch is accommodated by tetragonal distortion of the alloy layers. X-ray diffraction has been used to investigate such structural features. The tetragonal distortion of $Si_{1-x}Ge_x$ alloy layers in sample MBE-26 is apparent in Fig. 2, which displays the (004) Bragg reflection for (a) a thick Ge epilayer, (b) the as-grown sample MBE-26, and (c) MBE-26 annealed at 1050 °C for 30 min. The broad alloy peak in Fig. 2(b) is shifted with respect to the unstrained (004) reflection b_0 by an amount which corresponds to a tetragonal distortion of 2.2%, in good agreement with classical elastic theory. The shoulder peaks seen on the broad alloy peak are unresolved satellites that account for the superlattice periodicity. After annealing, the superlattice structure is destroyed and the x-ray diffraction spectrum corresponding to a dilute alloy ($x \simeq 0.09$) is obtained.

The Raman scattering measurements were carried out using the 90° scattering geometry depicted in Fig. 3. This configuration, which is nearly back-scattering *inside* the sample, resulted in low stray light intensities and allowed measurement of the Raman spectrum at frequency shifts less than 4 cm^{-1}. For most samples the spectra were excited with 300 mW of 4579-Å argon-laser light and with $\theta = 12.3° \pm 0.5°$, which corresponds to Brewster's angle at

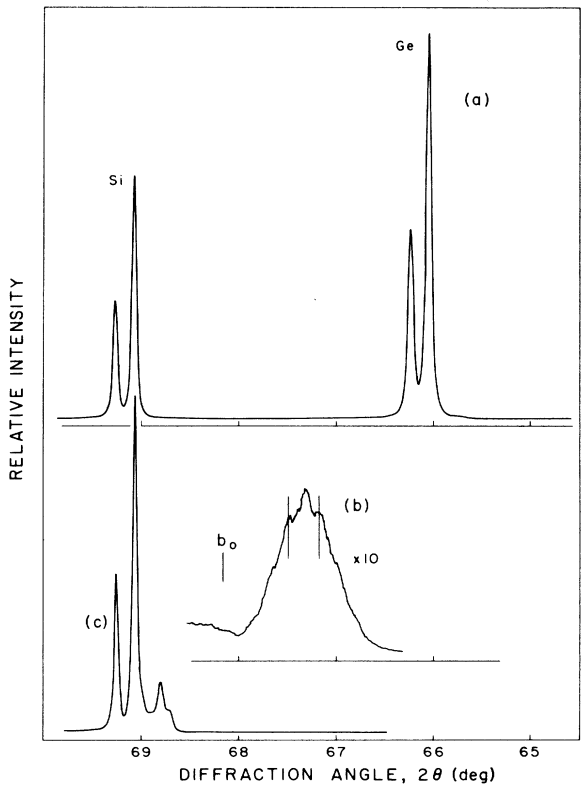

FIG. 2. X-ray diffraction profiles about the (400) reflection for (a) a thick epitaxial Ge layer (1.2 μm) grown on (100) Si, (b) superlattice MBE-26, (c) superlattice MBE-26 after annealing at 1050 °C for 30 min.

FIG. 1. A [110] cross-sectional TEM micrograph of superlattice MBE-44. The inset displays the corresponding diffraction pattern near the ($\bar{1}11$) position. Satellites along the growth direction (arrow) are due to the short superlattice modulation.

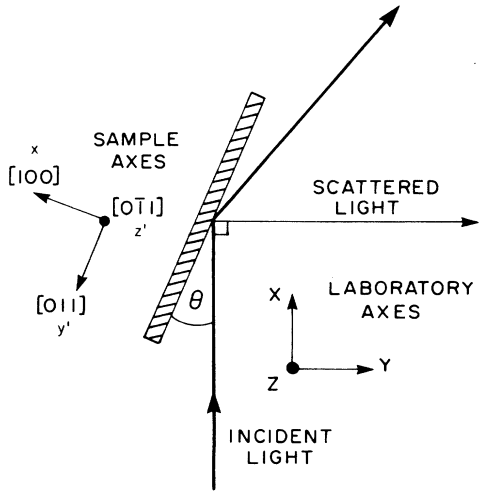

FIG. 3. The scattering geometry used in the Raman experiments.

this wavelength. Under these conditions, and for $X(YZ+YX)Z$ polarization [corresponding closely to $x(y'z'+y'y')\bar{x}$ polarization *within* the sample] which avoided absorption of the scattered light by the Polaroid polarization analyzer, the maximum Raman signal was obtained from the superlattice with respect to any substrate signal. This is because the sampling depth D, where 90% of the incident light intensity has been absorbed, is comparatively small (see Table II). The optical parameters given in Table II were deduced by interpolating between known values at nearby wavelengths.[12] In accordance with the D values given in this table, the acoustic phonon signal reduced in relative intensity with increasing laser wavelength and it could not be observed at the red wavelengths (where D is very large). The polarization, θ and λ dependences of the Raman scattering were studied in detail for sample MBE-17. The scattered light was analyzed with a Spex 14018 double monochromator, detected with a cooled RCA 31034A photomultiplier, and recorded under computer control.[13] All measurements were carried out at 295 K in a helium-gas atmosphere, which was used to eliminate air features from the spectrum.

IV. RESULTS AND DISCUSSION

In this section we present details of the observed Raman spectra and their interpretation. Data are presented first for samples MBE-35, -43, and -44 for the laser wavelength $\lambda=4579$ Å. Sample MBE-17 is then discussed in greater detail, viz., dependence on wavelength, polarization, scattering angle, and effects of annealing. Finally, the data for samples MBE-26 and -37 are presented for excitation with $\lambda=4579$ Å.

A. Samples MBE-35, -43, and -44

Raman spectra for these samples are shown in Fig. 4. Sample 35 shows ten well-resolved lines (Table III) for scattering with laser light of wavelength $\lambda=4579$ Å. At this wavelength the scattered momentum $q_p \simeq 0.8 q_{mz}$, i.e., well within the Brillouin zone. The spectrum is qualitatively similar to some of the published GaAs/AlAs superlattice spectra (see, for example, Refs. 4 and 5). The lines are very sharp, as is usual for acoustic modes, and their widths are resolution limited in these Raman measurements.

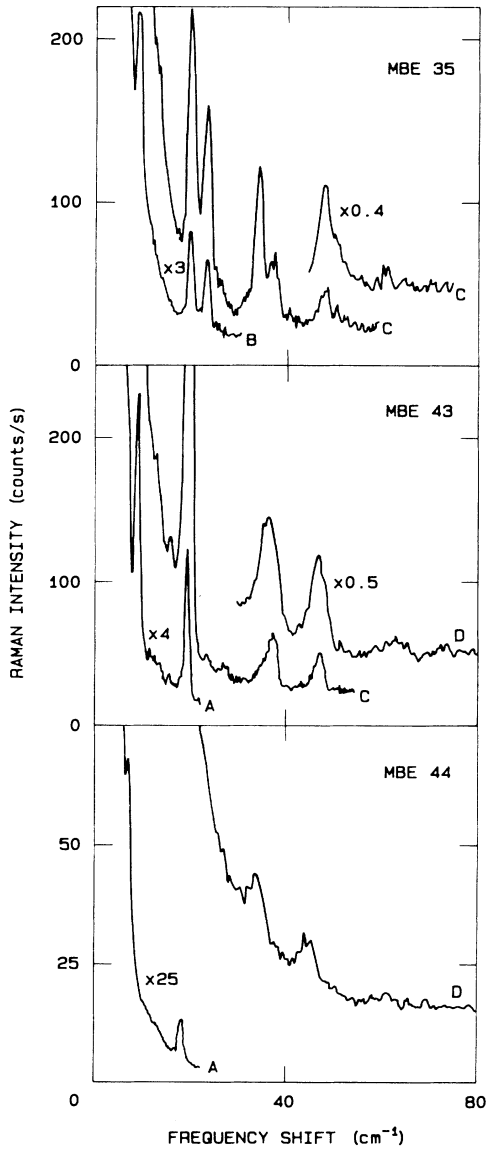

FIG. 4. Raman spectra of MBE-35, -43, and -44 recorded in $X(YZ+YX)Y$ polarization. Labels A, B, C, and D refer to experimental resolutions of 0.8, 1.1, 1.6, and 3.1 cm^{-1}, respectively. The intensities have been corrected for the slit width effect, using a standard resolution of 1.6 cm^{-1}.

TABLE II. Estimates for the optical parameters of Si at the laser wavelengths used in this study.

Laser wavelength λ (Å)	Refractive index η	Absorption coefficient α (cm^{-1})	Sampling depth D (Å)
4579	4.595	35 800	6440
4765	4.445	24 600	9370
4880	4.370	20 400	11 300
5145	4.225	14 700	15 700
6479	3.855	3240	71 000
6764	3.811	2540	91 000

The experimental frequency shifts, $\Delta\omega_{\text{expt}}$, given in Table III (and elsewhere) have an absolute instrumental error of ± 0.5 cm^{-1}. The weak lines are larger $\Delta\omega_{\text{expt}}$ may have larger uncertainties. The agreement between calculated[14] and observed peak positions is excellent except for the last three peaks of intensity less than 10. The disagreements for these higher-frequency peaks are greater than those resulting from errors (<0.1 cm^{-1}) in linearizing the Rytov model for $\omega < 100$ cm^{-1}. The experimental intensities are given in units of photomultiplier counts/s under standard conditions of 300 mW excitation at 476.5 nm, a resolution of 1.6 cm^{-1} (100 μm slit width),

TABLE III. Experimental and calculated Raman peaks and intensities for sample MBE-35, with $d_1=149$ Å, $d_2=43$ Å, and $x=0.3$. The calculated intensity is normalized to agree with the mean experimental intensity for folding index $m=1$. The value of I_{calc} has been rounded to the nearest 10 for $I_{calc}>10$.

m	$\Delta\omega_{expt}$ (cm^{-1})	$\Delta\omega_{calc}$ (cm^{-1})	I_{expt} (counts/s)	I_{calc}
0	5.4	5.4	2000	
1*a*	9.0	8.8	260	200
1*b*	20.0	19.5	170	200
2*a*	23.3	22.9	120	120
2*b*	34.3	33.7	96	120
3*a*	37.1	37.1	40	40
3*b*	47.6	47.9	22	40
4*a*	50.9	51.2	9	4
4*b*	60.8	62.0	5	4
5*a*	64.3	65.4	2	3
5*b*		76.2		3

and $\theta=12.3°$. The calculated intensities are obtained using the formula

$$I \propto m^{-2}\sin(m\pi d_1/d)\omega_m(n_m+1) \quad (8)$$

with the $\omega_m(n_m+1)$ Bose factor ignored. The calculated intensities, I_{calc}, listed in Table III are normalized to the mean experimental intensity of the $m=1$ doublet and rounded to the nearest 10 (for $I>10$). The general agreement between theory and experiment confirms the essential validity of Rytov's model and the photoelastic mechanism for light scattering[4] in these superlattices.

Samples 43 and 44, for which $q_p\simeq 0.8q_{mz}$ at $\lambda=4579$ Å, were specially prepared to have approximately equal layer thicknesses since, by Eq. (8), when $d_1=d_2=d/2$ the even-m peaks should be absent. This feature was indeed noted in the observed spectra (Fig. 4) which agree quite well with the calculated spectra (Tables IV and V). A number of weak features were observed for sample 43 in the regions where the "missing" peaks are expected to be, but they were too numerous to be entirely explainable in terms of the scattering from folded phonons with wave vector q_p. Some of the more prominent weak features corresponded to frequencies that could arise from scattering due to zone center (ZC) (i.e., $q=0$) or minizone edge (ZE) ($q=\pi/d$) phonons. These are also indicated in Table IV, and marked ZC ($q=0$) and ZE ($q=\pi/d$), respectively. They do not correspond to the frequencies of possible transverse modes. Microscopic examination of the crystal (MBE-43) showed that the crystal is a relaxed superlattice with misfit dislocations at the interfaces. This could explain the presence of the weak features observed in the spectrum. Another likely explanation for the appearance of weak lines at frequencies corresponding to acoustic phonons with $q\simeq 0$ is the presence of near-forward scattering, as found recently in GaAs/AlAs superlattices.[15] Such Raman scattering can occur under our experimental conditions due to partial reflections of the incident light at the alloy—Si-layer interfaces. The associated $q_p\simeq 0.01q_{mz}$ and the scattering would be weak, in agreement with experiment. However the weak peak at 16.6 cm^{-1} observed for sample 44 (Table V) cannot be correlated with any of these possible mechanisms.

TABLE IV. Experimental and calculated Raman peaks and intensities for sample MBE-43, with $d_1=d_2=97$ Å and $x=0.2$. The peaks corresponding to $m=2$ and 4, placed in parentheses, are of negligible intensity and are not observed. Other weak features are observed and can be correlated with zone center (ZC) and minizone edge (ZE) scattering. I_{calc} is scaled to the observed mean intensity of the $m=1$ doublet.

m	$\Delta\omega_{expt}$ (cm^{-1})	$\Delta\omega_{calc}$ (cm^{-1})	I_{expt} (counts/s)	I_{calc}
0	5.4	5.3	2900	
(ZE)	7.0	6.9	150	
1*a*	9.0	8.5	580	490
(ZC)	13.7	13.8	35	
1*b*	19.3	19.1	400	490
2*a*		(22.4)		0
(ZC)	26.8	27.7	9	
2*b*		(33.0)		0
(ZE)	34.3	34.6	7	
3*a*	36.8	36.2	36	60
3*b*	47.0	46.8	25	60
4*a*		(50.0)		0
4*b*		(60.7)		0
5*a*	63.0	63.9	5	2
5*b*	73.0	74.5	3	2

B. Sample MBE-17

This sample was studied in great detail since its period d was such that the scattering vector could be conveniently varied to probe the crystal inside ($q_p<q_{mz}$) and outside ($q_p>q_{mz}$) the minizone.

We have used four laser wavelengths; 5145, 4880, 4765, and 4579 Å for which q_p/q_{mz} becomes 0.89, 0.97, 1.01,

TABLE V. Experimental and calculated Raman peaks and intensities for sample MBE-44, with $d_1=102$ Å, $d_2=103$ Å, and $x=0.2$. Peaks corresponding to $m=2$ and 4 are in parentheses as they are predicted to have negligible intensity.

m	$\Delta\omega_{expt}$ (cm^{-1})	$\Delta\omega_{calc}$ (cm^{-1})	I_{expt} (counts/s)	I_{calc}
0	5.4	5.3	2300	
1*a*	7.1	7.8	450	200
?	16.6	?	25	
1*b*	18.2	18.4	200	200
2*a*		(20.9)		0
2*b*		(31.5)		0
3*a*	33.7	34.0	12	20
3*b*	44.0	44.6	8	20
4*a*		(47.1)		0
4*b*		(57.7)		0
5*a*	60.5	60.2	3	8
5*b*		70.8		8

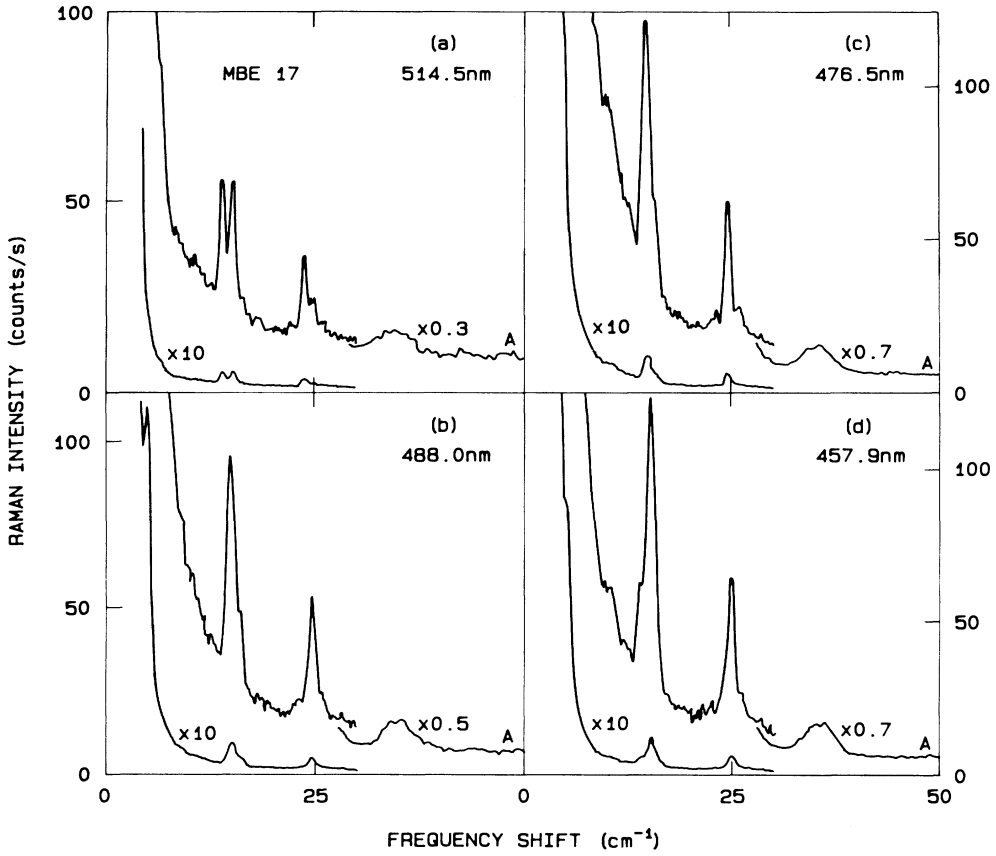

FIG. 5. Raman spectra of MBE-17 recorded in $X(YZ+YX)Y$ polarization using wavelengths of (a) 5145, (b) 4880, (c) 4765, and (d) 4579 Å and a slit width of 50 μm (200 μm for curve A). The corresponding spectral resolutions are (a) 0.6 (2.5), (b) 0.7 (2.7), (c) 0.7 (2.9), and (d) 0.8 (3.1) cm^{-1}.

and 1.09, respectively. Since $q_p < q_{mz}$ for the two longer wavelengths, normal Raman scattering is expected. For the two shorter wavelengths q_p is replaced by $\tilde{q}_p$ [Eq. (7)] and the scattering is umklapp assisted. Typical spectra are given in Fig. 5.

In Table VI we give the experimental and calculated results for the four wavelengths considered. The first column labeled m gives the zone folding index (except for the case marked $X+U$, to be discussed below) for the two cases where $q_p < q_{mz}$. For $\lambda = 5145$ Å, where $q_p/q_{mz} = 0.89$, the doublets (e.g., $1b,2a$) are sufficiently well separated and the agreement between the calculated $\Delta\omega$ and the experimental peaks (allowing for the basic instrumental error of ± 0.5 cm^{-1}) is excellent. The calculated intensities have been normalized to the mean experimental intensity (the experimental error is $\pm 12\%$) of the $1a,1b$ peaks and rounded to the nearest 10. The agreement is good. For $\lambda = 4880$ Å, where $q_p/q_{mz} = 0.97$, the a,b doublets are not resolvable. The experimental intensities given in the eighth column agree with the sum of the calculated intensities of the overlapping lines.

For $\lambda = 4765$ and 4579 Å, $q_p > q_{mz}$ and the peaks do not order monotonically in the m index (ninth column of Table VI). The reduced scattering vector $\tilde{q}_p$ is obtained by folding over the q_p into $\tilde{q}_p$ using Eq. (7), as shown in Fig. 6. This is equivalent to changing the phonon branch by ± 1 depending on whether the initial vector q_p was an a or b branch (e.g., $1a \rightarrow 0$, $0 \rightarrow 1a$, $2a \rightarrow 1b$, $2b \rightarrow 3a$, etc., see Fig. 6). If the m index of the ninth column is similarly changed to give $\tilde{m}$, then $\tilde{m}$ is now a monotonic sequence identical to the first column. The intensities of the observed lines for $q_p > q_{mz}$, calculated using $\tilde{m}$ would then be identical to that given in the fourth column. If m (ninth column) is used instead they will merely be rearranged. In either case the extremely high intensity of the line at 15.6 cm^{-1} for $\lambda = 4579$ Å or, equivalently, the line at 15.1 cm^{-1} for $\lambda = 4765$ Å requires explanation. Even the line at 24.7 cm^{-1} could be judged to be more intense than expected but this is not so evident as the accentuated intensity at 15.5 cm^{-1}.

We suggest that the enhancement at 15.5 cm^{-1} arises from umklapp processes whereby the Brillouin peak (BP) at $\Delta\omega_{BP} = q_p V_{SL} = 5.5$ cm^{-1} is shifted to $(q_p + G_{mz})V_{SL}$, giving $\Delta\omega = 15.55$ cm^{-1} for $\lambda = 4579$ Å and 15.05 cm^{-1} for $\lambda = 4765$ Å. Since the position of the Brillouin peak on the dispersion curve has already been obtained by the reduction $\tilde{q}_p = |q - G_{mz}|$, the observed enhancement at 15.5 cm^{-1} implies that momentum transfers correspond-

TABLE VI. Experimental and calculated Raman peaks (in cm^{-1}) and intensities (in counts/s) for sample MBE-17, with $d_1=225$ Å, $d_2=50$ Å, and $x=0.2$. The wavelength is varied to take the photon scattering vector q_p from inside the minizone to the outside. When $q_p > q_{mz}$ the ordering of the peaks does not follow the folding index m, due to the umklapp folding of q_p to $\tilde{q}_p$ (see Fig. 6). The row marked $X+U$ is explained in the text. The fourth column, I_{calc}, is normalized to the mean I_{expt} for the $m=1$ doublet.

	$q_p/q_{mz}=0.89$, $\lambda=5145$ Å			0.97, 4880 Å			1.01, 4765 Å			1.09, 4579 Å		
m	$\Delta\omega_{expt}$	$\Delta\omega_{calc}$	I_{calc}	I_{expt}	$\Delta\omega_{expt}$	$\Delta\omega_{calc}$	I_{expt}	m	$\Delta\omega_{expt}$	$\Delta\omega_{calc}$	I_{expt}	$\Delta\omega_{expt}$	$\Delta\omega_{calc}$	I_{expt}
0	4.4	4.5		460	4.9	4.9	520	1a	5.1	5.0	620		4.6	
1a	5.3	5.6	30	20		5.2		0		5.1		5.5	5.5	500
								X+U	10.0	10.1	6	10.5	10.1	10
1b	14.3	14.5	30	30	15.0	14.9	66	2a	15.1	15.0	82	14.4	14.6	18
2a	15.5	15.6	20	30		15.2		1b		15.2		15.6	15.5	103
					16.2		12		16.2		15			
					23.0		5		23.2		6			
2b	24.1	24.6	20	20	24.6	25.0	37	3a	24.8	25.1	43	24.7	24.7	47
3a	25.4	25.7	10	7		25.3		2b		25.2		26.6	25.6	7
					26.0		5		26.2		6			
3b		34.6	10			35.1		4a	35.1	35.1		35.1	34.7	8
4a		35.7	4			35.3		3b		35.3		36.3	35.6	4
4b		44.7	4			45.1		5a	45.0	45.2		44.8	44.8	
5a		45.8	0.3			45.4		4b		45.3		46.0	45.7	

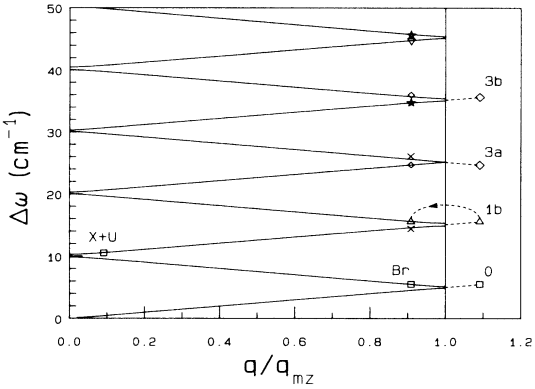

FIG. 6. The dispersion curve for MBE-17 calculated according to Rytov's theory, showing the folding of the photon wave vector into the minizone. The points inside the minizone are the experimental results for excitation at 4579 Å. The experimental point at 15.5 cm^{-1} (reduced wave vector $q/q_{mz}=0.91$) shown as a triangle corresponds to the triangle denoted by $1b$ at $q/q_{mz}=1.09$. Similarly, the two points marked as diamonds inside the minizone correspond to the $3a$ and $3b$ doublet.

ing to both $\tilde{q}_p = |q \pm G_{mz}|$ are manifested in the observed spectrum. In effect, we have two processes leading to almost the same shifted frequency.

Now we consider the row marked $X+U$ in Table VI (see also Fig. 6). We observe a peak at 10.2 cm^{-1} and at 10.5 cm^{-1} for the two cases where $q_p > q_{mz}$, but the structure disappears for wavelengths such that $q < q_{mz}$. This line seems to arise from possibly momentum nonconserving scattering near the zone center (ZC), viz., the $q \simeq 0$, $m=1$ ($\omega=10.1$ cm^{-1}) region. Since the peak is observed only for $q_p > q_{mz}$, we have designated it $X+U$ where X denotes an unknown process and U indicates the need for umklapp. A number of other weak features were also observed, both for $q_p/q_{mz}=0.97$ and 1.01, but not at laser wavelengths such that $q_p/q_{mz}=0.89$ and 1.09 (see Table VI). These weak lines which arise when $q_p \approx q_{mz}$ may also correspond to momentum nonconserving processes or to states at the minigaps.

Since the experimental geometry allows a small amount of transverse coupling we made careful studies of the spectrum for variation of the incident angle θ, in the range $1° < \theta \leq 25°$. No new peaks or features were observed that could be attributed to transverse acoustic modes. The previously identified features were very weakly dependent on the incident angle and small variations in frequency could be entirely ascribed to the effect of small wave-vector corrections to Eq. (5). The intensities of the acoustic modes relative to the intensity of the Si-layer optic phonon at 520 cm^{-1} did not vary with θ.

The polarization dependence of the main peaks in the spectrum of sample 17 is summarized in Fig. 7. The scattering is strongest in $X(YX)Y$ and $X(ZZ)Y$ polarizations; weak in $X(ZX)Y$; and not visible at all in $X(YZ)Y$. The scattering geometry of Fig. 3 shows that the sample $\{011\}$ faces are aligned parallel or perpendicular to the plane of scattering. This means that inside the crystal,

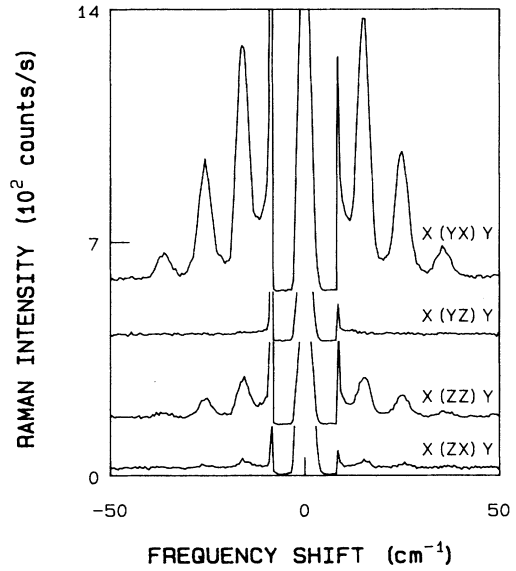

FIG. 7. The polarization dependence of the Raman spectrum of MBE-17 recorded using a wavelength of 4579 Å and a resolution of 3.1 cm^{-1}.

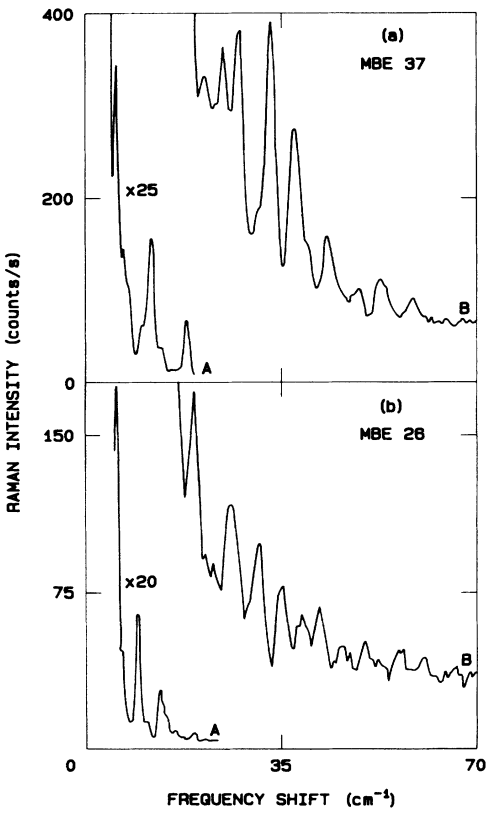

FIG. 8. Raman spectra of MBE-37 and -26 recorded in $X(YZ+YX)Y$ polarization at resolutions of 0.8 and 1.6 cm^{-1} (traces A and B, respectively). The intensity of trace A has been corrected for the slit width effect.

where quasi-back-scattering occurs, the $X(YX)Y$ and $X(ZZ)Y$ polarizations correspond closely to $x(y'y')\bar{x}$ and $x(z'z')\bar{x}$ polarizations, respectively, while the $X(ZX)Y$ and $X(YZ)Y$ polarizations correspond to $x(z'y')\bar{x}$ and $x(y'z')\bar{x}$, respectively. Thus the $q\neq 0$ folded acoustic modes all have A_1 symmetry, in agreement with theoretical predictions (see Sec. II). The appearance of some weak scattering in $X(ZX)Y$ polarization can be attributed to the imperfect back-scattering conditions.

C. Samples MBE-37 and -26

Sample 37 is a large period ($d_1=300$ Å, $d_2=110$ Å) superlattice with $x=0.45$. This is a highly strained superlattice where the concentration corresponds to that suggested to be optimal for ordering to occur in the Ge_xSi_{1-x} alloy layers.[16] Sample 26 has thicker layers ($d_1=450$ Å, $d_2=200$ Å) and a lower germanium concentration, viz., $x=0.33$. The Raman spectra of both crystals (Fig. 8)

TABLE VII. Calculated and experimental Raman peaks and intensities for sample MBE-26, with $d_1=450$ Å, $d_2=200$ Å, and $x=0.33$. I_{calc} is normalized to the observed intensity of the peak labeled 1b. The row marked (ZC) gives the zone center frequency nearest to the observed peak at 16.1 cm^{-1}.

m	ω_{expt} (cm^{-1})	ω_{calc} (cm^{-1})	I_{expt} (counts/s)	I_{calc}
0	5.5	5.3	2800	
3a	6.7	7.0	360	90
1b	9.4	9.4	1085	1085
4a	11.0	11.1	160	3
2b	13.5	13.5	510	510
5a	14.4	15.2	70	60
(ZC)	16.1	16.5	55	
3b	17.4	17.6	25	90
6a	19.7	19.4	75	60
4b	21.4	21.7	20	3
7a	23.3	23.5	17	10
5b	26.3	25.8	60	60
8a		27.6		3
6b	31.2	29.9	60	60
9a		31.7		20
7b		34.1		10
10a	35.3	35.8	40	20
8b		38.2		3
11a	39.3	39.9	30	3
9b	42.1	42.3	35	20
12a		44.0		3
10b	46.3	46.4	16	20
13a		48.1		10
11b	49.9	50.5	20	3
14a		52.2		9
12b		54.6		3
15a	56.6	56.3	16	1
13b		58.7		12
16a	60.2	60.4	14	3
14b		62.8		9
17a	64	64.5	6	7
15b	66	66.9	8	1

TABLE VIII. Calculated and observed Raman peaks and intensities for sample MBE-37, with $d_1=300$ Å, $d_2=110$ Å, and $x=0.45$. ZC and ZE refer to the zone center and zone edge frequencies nearest to $\Delta\omega_{expt}$. I_{calc} is normalized to agree with I_{expt} for the peak 1*b*.

m	$\Delta\omega_{expt}$ (cm^{-1})	$\Delta\omega_{calc}$ (cm^{-1})	I_{expt} (counts/s)	I_{calc}
0	5.5	5.2	5700	
(ZC)	6.8	6.5	900	
2*a*	7.8	7.6	1450	1700
(ZE)	10.2	9.7	900	
1*b*	11.8	11.6	3800	3800
3*a*	13.7	14.0	450	250
(ZE)	15.5	16.2	90	
2*b*	18.4	18.1	1450	1700
4*a*	21.5	20.5	60	20
3*b*	25.0	24.5	130	250
5*a*	27.6	26.9	190	220
4*b*		30.9		20
6*a*	33.5	33.3	250	180
5*b*	37.8	37.3	150	220
7*a*		39.7		20
6*b*	43.7	43.7	70	180
8*a*		46.1		20
7*b*	49.0	50.2	30	20
9*a*	53.0	52.6	40	90
8*b*		56.6		20
10*a*	59.0	59.0	30	50

are extraordinarily rich in detail, with many peaks, and at least in appearance quite unlike the GaAs/AlAs spectra so far published.

For Raman scattering with laser light of wavelength $\lambda=4579$ Å, $q_p/q_{mz}\simeq 1.63$ and 2.58 for MBE-37 and -26, respectively. In Table VII we compare the calculated and observed spectra for MBE-26. Over 30 Raman peaks were observed for $\Delta\omega \lesssim 65$ cm^{-1} and they agree well with the calculations, which identified scattering from folding index *m* as high as 17. A somewhat weak line observed at 16.1 cm^{-1} cannot arise from folded phonons with quasi-momentum conservation. The observed peak may be identified with a zone center (ZC) phonon from a momentum nonconserving process.

The spectrum of MBE-37 is also quite rich and interesting. As shown in Table VIII, all of the principal peaks are very well explained by the Rytov model. However, of the 17 observed peaks, there are four less intense peaks that do not fit into the present scheme. Calculations show that they cannot be explained by invoking scattering from transverse modes. These peaks are very close to the zone center (ZC) and zone edge (ZE) frequencies as shown in Table VIII and may arise from momentum nonconserving processes.

V. CONCLUSIONS

We have presented a detailed study of Raman scattering from folded longitudinal acoustic modes in Si/Ge_xSi_{1-x} strained-layer superlattices. Rytov's theory of acoustic vibrations in layered media is found to accurately model the observed spectra.

By taking advantage of the possibility of growing thick layer (large period) superlattices, we have been able to probe the interior and exterior regions of the mini-Brillouin-zone. These studies have led to the observation of umklapp-mediated Brillouin and Raman scattering peaks—processes which are impossible to observe by light scattering in an ordinary bulk crystal.

[1]A. S. Barker, Jr., J. L. Merz, and A. C. Gossard, Phys. Rev. B **17**, 3181 (1978).
[2]C. Colvard, R. Merlin, M. V. Klein, and A. C. Gossard, Phys. Rev. Lett. **45**, 298 (1980).
[3]J. Sapriel, J. C. Michel, J. C. Tolédano, R. Vacher, J. Kervarec, and A. Regreny, Phys. Rev. B **28**, 2007 (1983).
[4]C. Colvard, T. A. Grant, M. V. Klein, R. Merlin, R. Fischer, H. Morkoc, and A. C. Gossard, Phys. Rev. B **31**, 2080 (1985).
[5]M. Nakayama, K. Kubota, T. Kanata, H. Kato, S. Chika, and N. Sano, Jpn. J. Appl. Phys. **24**, 1331 (1985).
[6]M. W. C. Dharma-wardana, D. J. Lockwood, J.-M. Baribeau, and D. C. Houghton, Phys. Rev. B **34**, 3034 (1986); Bull. Am. Phys. Soc. **31**, No. 3, 348 (1986).
[7]S. K. Yip and Y. C. Chang, Phys. Rev. B **30**, 7037 (1984).
[8]S. M. Rytov, Akust. Zh. **2**, 71 (1956) [Sov. Phys.—Acoust. **2**, 68 (1956)].
[9]S.-Y. Ren and W. A. Harrison, Phys. Rev. B **23**, 762 (1981), see their Table III.
[10]See, for example, J. C. Bean, Mater. Res. Soc. Symp. Proc. **37**, 245 (1985).
[11]H. Brugger, G. Abstreiter, H. Jorke, H. J. Herzog, and E. Kasper, Phys. Rev. B **33**, 5928 (1986).
[12]D. F. Edwards, in *Handbook of Optical Constants of Solids,* edited by E. D. Palik (Academic, New York, 1985), p. 547.
[13]N. L. Rowell, D. J. Lockwood, and P. Grant, J. Raman Spectrosc. **10**, 119 (1981).
[14]The layer thicknesses d_1 and d_2 given in Table III used to obtain these results vary slightly from those found by TEM, as listed in Table I. The differences are within the experimental error.
[15]B. Jusserand, F. Alexandre, J. Dubard, and D. Paquet, Phys. Rev. B **33**, 2897 (1986).
[16]A. Ourmazd and J. C. Bean, Phys. Rev. Lett. **55**, 765 (1985).

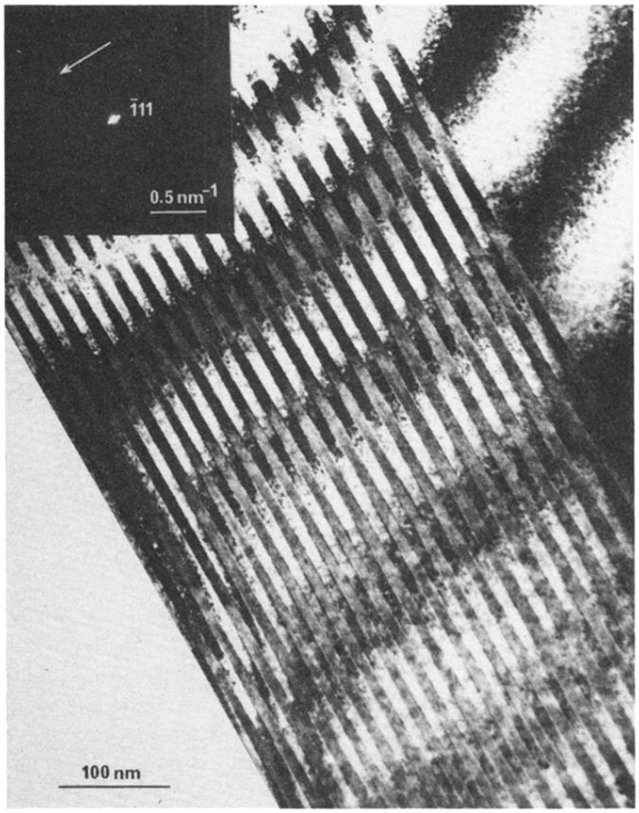

FIG. 1. A [110] cross-sectional TEM micrograph of superlattice MBE-44. The inset displays the corresponding diffraction pattern near the ($\bar{1}11$) position. Satellites along the growth direction (arrow) are due to the short superlattice modulation.